

Cite this: *RSC Adv.*, 2015, 5, 12583

# Electrochemical performance improvement of N-doped graphene as electrode materials for supercapacitors by optimizing the functional groups†

Wei Li,<sup>‡abc</sup> Hong-Yan Lü,<sup>‡b</sup> Xing-Long Wu,<sup>\*ab</sup> Hongyu Guan,<sup>b</sup> Ying-Ying Wang,<sup>ab</sup> Fang Wan,<sup>ab</sup> Guang Wang,<sup>b</sup> Li-Qun Yan,<sup>d</sup> Hai-Ming Xie<sup>ab</sup> and Rong-Shun Wang<sup>\*ab</sup>

Graphene material prepared by reducing graphene oxide (GO, prepared by the modified Hummers method) has been considered as one of the most promising candidates for electrode materials for supercapacitors due to its mass producibility, high electrical conductivity, large specific surface area, and superior mechanical strength. However, it usually exhibits an unfavorable cycling performance, mainly large capacitance fading in the initial thousands of cycles, as shown but not discussed in some previous reports. In this paper, we not only find a similar phenomenon to a commercial graphene material, but also develop a very simple method to successfully enhance its electrochemical properties in terms of cycle life as well as high-rate performance, leakage current and alternating current impedance. For example, the relatively low capacitance retention of about 89.9% at the initial 1000<sup>th</sup> cycle was increased up to 99.7% after improvement, the capacitance retention was raised to 73% from 43% at a scan rate of 100 mV s<sup>-1</sup> in cyclic voltammetry, and leakage current density was significantly more than halved (from 2.42 mA g<sup>-1</sup> to 1.01 mA g<sup>-1</sup>). Additionally, the reasons for the improvement are also disclosed by analyzing the characterization results of X-ray photoelectron spectroscopy, electrochemical impedance spectroscopy, X-ray diffraction, Fourier transform infrared spectroscopy and Raman spectroscopy. It is found that the optimization of the functional groups of doped nitrogen and oxygen atoms may contribute to the improvement of cycle life and decrease of leakage current density, and the enhanced rate performance can be attributed to the increase of electrical conductivity.

Received 15th October 2014

Accepted 5th January 2015

DOI: 10.1039/c4ra12383b

www.rsc.org/advances

## 1. Introduction

In recent years, considerable attention has been focused on more efficient energy storage devices with a fast charge and discharge ability to relieve the pressures of increasing oil demand, depletion of non-renewable resources, and environmental pollution.<sup>1–3</sup> Among these devices, supercapacitors (SCs), also called electrochemical capacitors (ECs), represents one of the developing directions of ultrafast charge/discharge,

and ultra-long cycle life.<sup>4–6</sup> On the basis of their energy storage mechanism, SCs are usually categorized into electrochemical double-layer capacitors (EDLCs) and pseudo-capacitors.<sup>7</sup> In EDLCs, the charges are mainly stored at the electrode/electrolyte interface by the charge separation of the electrode solution, which is very different from the multielectron-transfer Faradic reaction based energy storage, which occurs in the pseudocapacitors. Thus, the capacitance of EDLCs is by and large proportional to the specific surface area of active electrode materials. Currently, most of the electrode materials, which are used in commercial SCs (mainly EDLCs) are carbonaceous materials,<sup>8–11</sup> because they are not only low-cost but also could be prepared with high specific surface area larger than 2500 m<sup>2</sup> g<sup>-1</sup>,<sup>12</sup> which could significantly increase the capacitance of SCs.

Among the various kinds of carbonaceous materials, graphene, which is a two-dimensional carbon nanostructure with a single sp<sup>2</sup>-carbon-atom thickness, has been considered as one of the most promising electrode material candidate for SCs due to its high electrical conductivity, very large specific surface area (theoretically ~2650 m<sup>2</sup> g<sup>-1</sup>), and superior mechanical strength.<sup>13–17</sup> For the large-scale preparation of graphene materials, the modified

<sup>\*</sup>National & Local United Engineering Lab for Power Battery, Northeast Normal University, Changchun, Jilin 130024, P. R. China. E-mail: xinglong@nenu.edu.cn; wangrs@nenu.edu.cn; Fax: +86-0431-85099128; Tel: +86-0431-85099128

<sup>b</sup>Faculty of Chemistry, Northeast Normal University, Changchun, Jilin 130024, P. R. China

<sup>c</sup>Institute of Chemical Technology, Changchun University of Technology, Changchun, Jilin 130021, P. R. China

<sup>d</sup>Beijing Carbon Century Technology Co., Ltd, Beijing 101400, P. R. China

† Electronic supplementary information (ESI) available: Photograph, FT-IR and Raman spectra, CV and galvanostatic charge/discharge curves, as well as O1s XPS profiles of the rGO-based samples. See DOI: 10.1039/c4ra12383b

‡ These authors contributed equally to this work.

Hummers method followed by a chemically reduced process has been proved to be the most efficient way compared with others,<sup>18</sup> such as mechanical stripping, epitaxial growth and chemical vapor deposition. Generally, the as-obtained graphene materials prepared by this method are named reduced graphene oxide (rGO). In the previous studies, it has been undoubtedly demonstrated that rGO usually exhibits more excellent electrochemical properties in terms of higher energy and power density compared to traditional porous carbon materials when used as the active electrode materials for SCs if the restacking of graphene layers is effectively inhibited.<sup>19,20</sup> For example, Ruoff and co-workers<sup>21</sup> increased the specific surface area of graphene-derived carbon materials to  $3100 \text{ m}^2 \text{ g}^{-1}$  by chemically activating graphene oxide, and significantly improved their gravimetric capacitance and energy density within both organic and ionic liquid electrolytes. The three-dimensional strutted graphene constructed by Wang *et al.*<sup>22</sup> could prevent the self-agglomeration of graphene sheets well, and enhance the specific capacitance as high as  $250 \text{ F g}^{-1}$  at a current density of  $1 \text{ A g}^{-1}$ . By the liquid electrolyte mediated method, Li and co-workers<sup>23</sup> optimized the ion-accessible surface of graphene materials, reduced the ion transport resistance in SCs, and hence increased the volumetric energy densities of graphene based SCs to  $60 \text{ Wh L}^{-1}$ .

In addition to energy and power densities, cycle life is another noteworthy factor for SCs evaluation, because SCs are traditionally famous for their ultra-long cycle life up to hundreds of thousands of cycles. However, we unfortunately find that most of the rGO based SCs exhibit an unfavorable cycling performance, which includes mainly large capacitance fading in the initial cycling processes, although the following cycles are relatively excellent.<sup>24–27</sup> For instance, the capacitance fading of the initial 500 cycles of a three-dimensional rGO aerogel is as high as  $\sim 10.3\%$  from  $\sim 145 \text{ F g}^{-1}$  of the 1<sup>st</sup> cycle to  $\sim 130 \text{ F g}^{-1}$  of the 500<sup>th</sup> cycle at a current density of  $10 \text{ A g}^{-1}$ , although that of the following thousands of cycles is only about  $0.002\%$  per cycle.<sup>25</sup> Therefore, to better realize the superiority of rGO based materials as active electrode materials for SCs, it becomes an urgent task to improve their cycle performance. Herein, we successfully developed a simple and mass-producible method to enhance the electrochemical properties of rGO based materials as electrode materials for SCs. This method cannot only improve the cycle performance, but also decrease the impedance and leakage current and hence enhance the high-rate capacitance and power density. It is noteworthy that the studied rGO is a commercial product, which promises the direct utilization of this method to commercial rGO materials and hence the development of more superior graphene products (see the images as shown in Fig. S1†) as electrode materials for SCs. Moreover, the possible reasons of improvements are also discussed based on the results of the structural characterization and electrochemical measurements.

## 2. Experimental section

### 2.1. Preparation of thermally stabilized rGO (TS-rGO)

Beijing Carbon Century Technology Co. Ltd. kindly provided a commercial rGO (C-rGO) product as the raw material, which was synthesized by the modified Hummers method followed by

a reduction process in aqueous solution. Note that the C-rGO is actually a nitrogen-doped rGO with a high nitrogen content of about  $4.5 \text{ wt}\%$  according to X-ray photoelectron spectroscopy (XPS) test results, because lots of carbon–nitrogen bonds are formed in the redox processes between GO precursors and the hydrazine reductant. For the preparation of the advanced graphene material with enhanced electrochemical properties, this nitrogen-doped C-rGO material was placed in a quartz tube and annealed at the proper temperature from  $500^\circ\text{C}$  to  $800^\circ\text{C}$  for 2 hours under high purity  $\text{N}_2$  containing  $5\% \text{ H}_2$ . A large number of samples could be collected after the temperature of the furnace cooled to room temperature. Thereafter, the improved C-rGO materials are named as thermally stabilized rGO (abbreviated as TS-rGO) or TS-rGO(A), in which A represents the heating temperature from  $500^\circ\text{C}$  to  $800^\circ\text{C}$ .

### 2.2. Structural characterization

The morphology of all the samples was first investigated by scanning electron microscopy (SEM, Philips XL30, operating at  $10 \text{ kV}$ ). Transmission electron microscopy (TEM) was carried out on a JEOL-2100 F at  $200 \text{ kV}$ . X-ray diffraction (XRD) patterns were recorded on a Rigaku D/max 2000 spectrometer using  $\text{Cu K}\alpha$  radiation ( $\lambda = 1.5406 \text{ \AA}$ ). Raman spectra were obtained using a Digilab FTS3500 (Bio-Rad) with a laser wavelength of  $632.8 \text{ nm}$ . X-ray photoelectron spectroscopy (XPS) was performed on a Thermo Scientific ESCALab 250Xi using  $200 \text{ W}$  monochromated  $\text{Al K}\alpha$  radiation. A  $500 \mu\text{m}$  X-ray spot was used for XPS analysis. The base pressure in the analysis chamber was about  $3 \times 10^{-10} \text{ mbar}$ . Typically, the hydrocarbon C1s line at  $284.8 \text{ eV}$  from adventitious carbon is used for energy referencing. Fourier transform infrared spectra (FT-IR) were measured on a Nicolet 6700. Particle size and distribution were tested on a Zetasizer NanoZS (Malvern Instruments). The  $\text{N}_2$  adsorption–desorption isotherms were measured at  $77.4 \text{ K}$  with a Micromeritics ASAP 2020 HD88 surface area analyzer.

### 2.3. Electrochemical measurements

The working electrodes were prepared by pressing a mixture of graphene-derived active materials and Teflonized acetylene black (TAB) binder at a weight ratio of  $90 : 10$  onto a  $316\text{L}$  stainless steel mesh and then drying in vacuum at  $100^\circ\text{C}$  for  $8 \text{ h}$ . The loading mass of active materials on the electrode substrate was *ca.*  $6\text{--}8 \text{ mg cm}^{-2}$ . The electrochemical properties of the prepared electrodes were carefully studied in both three-electrode and two-electrode symmetric systems in  $1 \text{ mol L}^{-1} \text{ H}_2\text{SO}_4$  electrolyte. While the cyclic voltammetry (CV) tests were performed in three-electrode cells using a platinum electrode ( $1 \times 1 \text{ cm}^2$ ) as the counter electrode and saturated calomel electrode (SCE) as the reference electrode, the galvanostatic cycling, leakage current test and electrochemical impedance spectroscopy (EIS) were carried out in two-electrode symmetric cells. The CVs (voltage range:  $-0.2$  to  $0.95 \text{ V vs. SCE}$ ; scan rate:  $2\text{--}100 \text{ mV s}^{-1}$ ) and EIS (frequency range:  $100 \text{ kHz}$  to  $0.01 \text{ Hz}$ ; amplitude:  $5 \text{ mV}$ ) were measured on a PARSTAT 4000 advanced electrochemical system (Princeton Applied Research). Galvanostatic cycling

tests were carried out on a LANHE 2001A system under different current densities in the voltage range of 0–1.2 V vs. SCE. Additionally, we also perform the galvanostatic charge/discharge tests in the electrolyte of 1 mol L<sup>-1</sup> H<sub>2</sub>SO<sub>4</sub> containing 0.1 mol L<sup>-1</sup> VOSO<sub>4</sub>/NH<sub>4</sub>VO<sub>3</sub> to increase the energy and power densities of the cells.

### 3. Results and discussion

The morphological and structural variations of C-rGO in the thermally stabilized processes were firstly characterized by the SEM, TEM, XRD, FT-IR, Raman and XPS technologies. As seen in the typical SEM image shown in Fig. 1a, the utilized C-rGO material is composed of uniform and wrinkled graphene layers, which is consistent with previously reported results.<sup>28–30</sup> After the thermally stabilized treatment, there was no obvious change in morphology (Fig. 1b), demonstrating that the heating process does not cause undesirable restacking and

aggregation. Fig. 1c further shows the TEM image of the TS-rGO(700) material, exhibiting obvious graphene layers with many wrinkles and twists, which is very similar to the reported TEM images of rGO materials. Because all of the TS-rGO samples obtained at various heating temperatures have similar SEM images, here we show the TS-rGO(700) one as an example. Fig. 2a compares the XRD pattern of C-rGO with those of all the TS-rGO materials. It can be seen that the main diffraction in all the XRD patterns is one broad peak at around 23–25°, which corresponds to the moderately aligned graphitic arrays along the (002) direction. However, the 2θ values (25.1°) of all the thermally stabilized rGO materials are obviously larger than that (23.8°) of pristine C-rGO, indicating the reduction of the interplanar distance of the crystal plane (002) after the heating treatment according to Bragg's equation. This originates from the decomposition and decrease of O-/N-based functional groups in the processes of the heating treatment, which was confirmed by the following XPS and FT-IR tests.

Fig. 2b shows the XPS survey spectra of all the samples. It can be clearly seen that all of the samples are composed of three elements, *i.e.*, carbon, oxygen and nitrogen. For the C-rGO raw material, the atomic ratio of C, O and N is about 83.89 : 12.07 : 4.04 as shown in Table 1. After thermal stabilization, the contents of the O and N heteroatoms are obviously decreased, and the higher the heating temperature, the lower the contents of the doping atoms. For example, the atomic percentages of O and N are about 7.04% and 1.81% in the TS-rGO(700) materials, respectively. In addition to the variations of the elemental contents and quantity of the functional groups, the chemical bonding states of the doping elements also changed in nature along with the process of thermal treatment, which significantly affects their electrochemical properties as electrode materials for SCs. For example, two weak FT-IR absorption bands located at about 1734 cm<sup>-1</sup> and 1655 cm<sup>-1</sup> (marked as asterisks in the inset of Fig. S2†) disappeared after the heating treatment, which indicates the disappearance or reduction of the corresponding chemical bonds. The relevance between the electrochemical properties and functional groups as well as chemical bonds will be discussed in the following sections with the help of fitting of the XPS profiles. Moreover, all the samples are further characterized by their Raman spectra as shown in Fig. S3.† The two characteristic peaks located at about 1320 and 1590 cm<sup>-1</sup> correspond to the D-band and G-band of carbonaceous materials, respectively. The peak intensity ratio of the D-band to G-band always remains at around 1.4 (Table S1†), demonstrating that the atomic and crystalline structures of most of carbon atoms are unchanged before and after the heating treatment.

The electrochemical properties of C-rGO and all of the TS-rGO samples as electrode materials for SCs were evaluated in both three and two electrode systems. Fig. 3a and b are the typical CV curves of C-rGO and TS-rGO(700), respectively. The test system used is a three-electrode system, in which a platinum plate of 1 × 1 cm<sup>2</sup> is the counter electrode, and a saturated calomel electrode (SCE) is the reference electrode. As

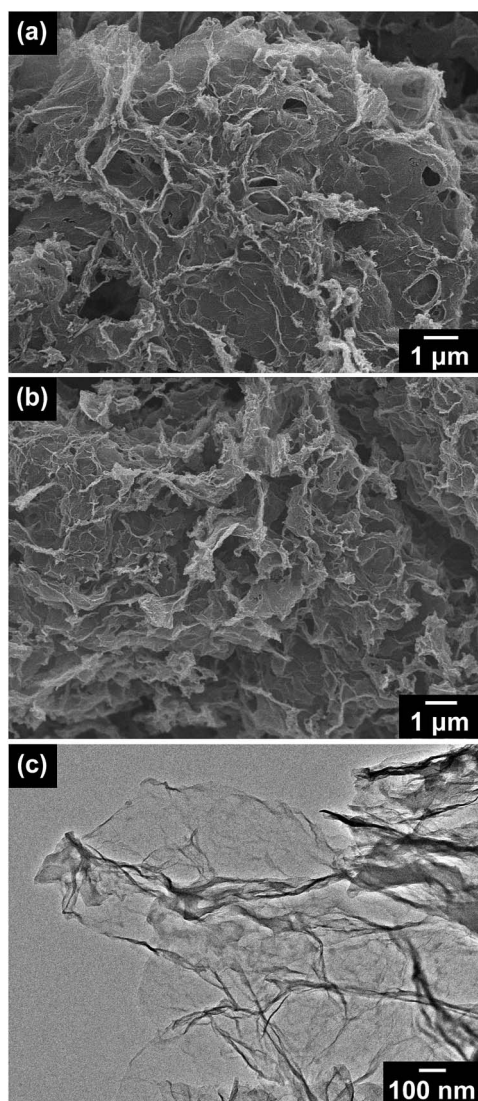


Fig. 1 SEM images of (a) C-rGO and (b) TS-rGO(700), and (c) TEM image of TS-rGO(700).



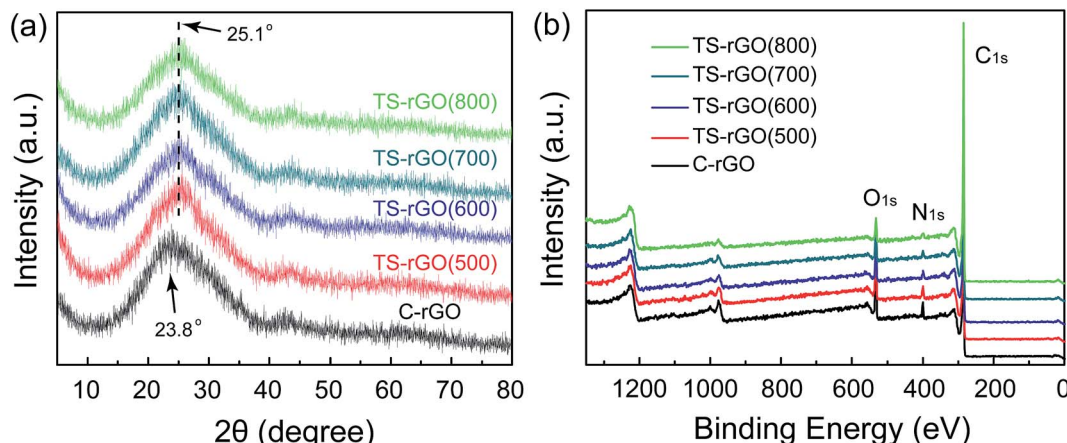
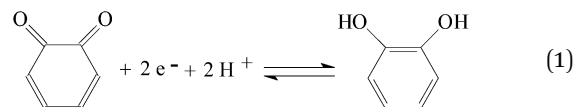


Fig. 2 (a) XRD patterns and (b) XPS survey spectra of pristine C-rGO and TS-rGO materials prepared at various temperatures from 500 °C to 800 °C.

Table 1 Elemental composition of C-rGO and TS-rGO materials calculated from the XPS survey

Samples	Atomic%		
	C	N	O
C-rGO	83.89	4.04	12.07
TS-rGO(500)	86.51	3.14	10.35
TS-rGO(600)	90.07	2.23	7.71
TS-rGO(700)	91.15	1.81	7.04
TS-rGO(800)	94.34	1.33	4.34

shown in Fig. 3a and b, both exhibit nearly rectangular shapes at a low scan rate of  $2 \text{ mV s}^{-1}$ . However, the CV curves of the C-rGO material quickly deviate from rectangle when the scan rate is higher than  $20 \text{ mV s}^{-1}$ , while those of the TS-rGO(700) material remain almost unchanged. This implies that the thermally stabilized rGO materials will exhibit a better rate performance compared to the pristine C-rGO material. Therefore, Fig. 3c further compares the capacitance retention along with the increase of the scan rate from  $1 \text{ mV s}^{-1}$  to  $100 \text{ mV s}^{-1}$ . All of the TS-rGO materials indeed display significantly improved capacitance retention, and the TS-rGO(700) material is the best one. The capacitance retention of the TS-rGO(700) material remains up to 73% when the scan rate increases to  $100 \text{ mV s}^{-1}$ , whereas that of the pristine C-rGO material is only 43%. Below  $700^\circ\text{C}$ , the capacitance retention increases with the rise of the heating temperature, because an elevated temperature could effectively improve the electrical conductivity of products. However, when the heating temperature further rises above  $700^\circ\text{C}$ , the rate performance begins to deteriorate. As shown in Fig. 3c, the capacitance retention of the TS-rGO(800) material is obviously lower than that of the TS-rGO(700) material when the scan rate is above  $20 \text{ mV s}^{-1}$ , although they are comparative below  $20 \text{ mV s}^{-1}$ . This may be due to the aggravation of detrimental aggregation and restacking of graphene layers at higher heating temperatures above  $700^\circ\text{C}$ , as demonstrated by the particle size distribution test shown in Fig. S5†



In addition to the rectangle-like shapes of the CV curves, the pseudocapacitive peaks, which appeared are another interesting issue worth attention and discussion. First, there is one pair of reversible peaks at around  $0.3\text{--}0.4 \text{ V vs. SCE}$  in all the CV curves of the C-rGO and TS-rGO materials, which is attributable to the oxidation/reduction of hydroquinone/quinone groups in acidic electrolyte (see eqn (1)) as confirmed by Andreas and Conway.<sup>31,32</sup> The difference between the potentials of the anodic and cathodic peaks ( $|\Delta E_{\text{p,a-p,c}}|$ ) in CV curves are usually employed to evaluate the reversibility of the corresponding pseudocapacitive reaction. At a low scan rate, the  $|\Delta E_{\text{p,a-p,c}}|$  values of all samples before and after thermal treatment are lower than  $100 \text{ mV}$ , which is close to  $59 \text{ mV}$ , hence demonstrating their high reversibility. However, the values of the C-rGO material increase sharply along with the increase of the scan rate, while those of the TS-rGO materials just increase slowly. Taking the scan rate of  $20 \text{ mV s}^{-1}$  as an example, as shown in Fig. 3a and b, the  $|\Delta E_{\text{p,a-p,c}}|$  value for the TS-rGO(700) material is about  $150 \text{ mV}$ , which is much smaller than that (about  $382 \text{ mV}$ ) for the pristine C-rGO material. This demonstrates that the thermally stabilized treatment processes can significantly improve the reversibility of the hydroquinone/quinone redox couples in the rGO based materials, especially at a scan rate above  $5 \text{ mV s}^{-1}$ , and hence further increase their high-rate capacitance (Fig. 3c). Additionally, there exist extra cathodic peaks at  $0\text{--}0.1 \text{ V vs. SCE}$  in the CV curves of the pristine C-rGO material compared to the TS-rGO materials as shown in Fig. 3a and b and S6†. Although these pseudocapacitive peaks could increase the specific capacitance of the materials, they are unfortunately unstable and irreversible. More specifically, these cathodic peaks move gradually to a higher potential with a lower peak current, and the corresponding anodic peaks cannot be found in the CV curves (Fig. S6a†). After thermal stabilization,

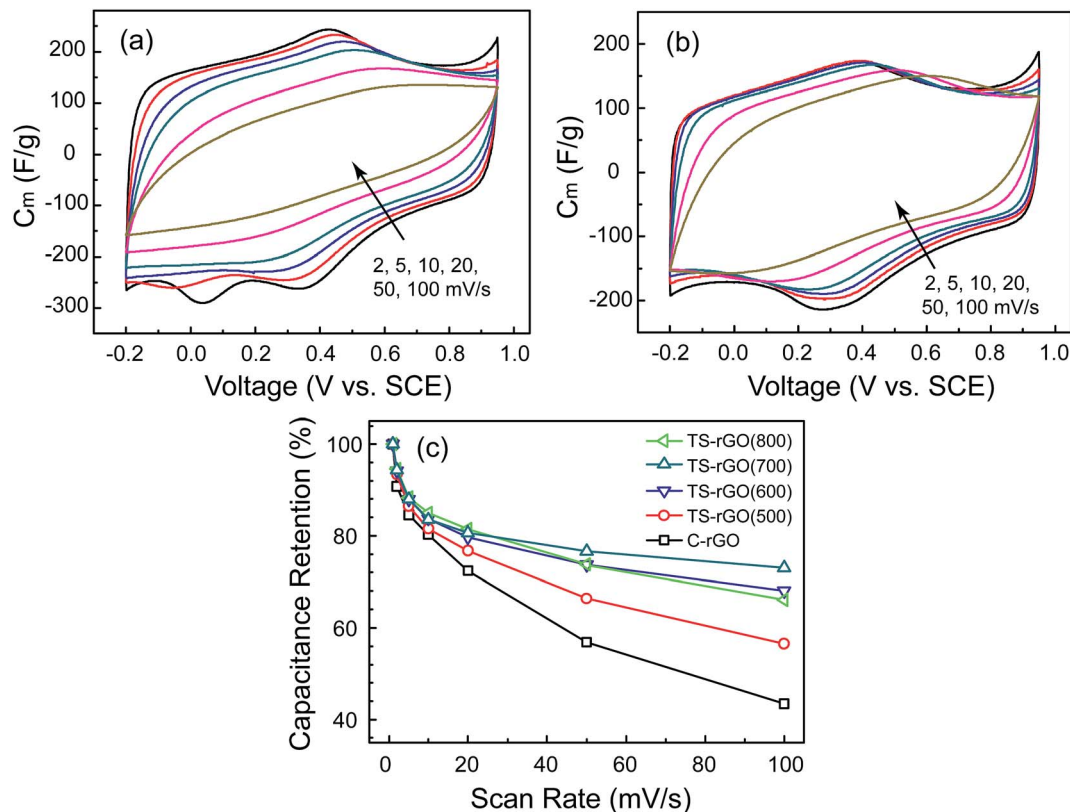


Fig. 3 CV curves of (a) C-rGO and (b) TS-rGO(700) materials at various scan rates from 2 to 100  $\text{mV s}^{-1}$ . (c) Capacity retention versus scan rate of C-rGO and TS-rGO materials.

these undesirable peaks disappear from the CV curves as shown in Fig. S6b,<sup>†</sup> implying that the TS-rGO materials will exhibit superior electrochemical stability.

The electrochemical properties of these rGO-based materials as electrode materials for SCs were further studied in symmetric two-electrode cells. Here, we take the TS-rGO(700) material as an example of thermally stabilized samples for comparison with the pristine C-rGO material, because the TS-rGO(700) material exhibits the best high-rate performance among all the TS-rGO materials, and the variation of electrochemical properties with heating temperature is similar to the CV test results. Fig. 4a first exhibits the galvanostatic charge/discharge curves of the TS-rGO(700) material at  $2 \text{ A g}^{-1}$  in the voltage range of 0–1.2 V, which is symmetric and linear, indicating its superior capacitance behaviour. Fig. 4b compares the cycle stability of the rGO based materials before and after the thermal treatment. For the pristine C-rGO material, the decay trend of the specific capacitance is analogous to some previously reported results,<sup>24–27</sup> i.e., rapid capacitance fading in the initial cycling processes followed by a relatively stable cycle life as discussed in the Introduction. As shown in Fig. 4b, the specific capacitance of the pristine C-rGO material decreases up to 10.1% in the initial 1000 cycles, a sharp and unfavorable decay of specific capacitance, which can be effectively avoided after thermal stabilization. The capacitance retention of TS-rGO(700) is up to 99.7% in the

initial 1000 cycles. These results are consistent with the CV test results (Fig. S6<sup>†</sup>) as discussed above. Fortunately, the specific capacitance of the pristine C-rGO material gradually reaches a relatively steady value in the following cycle process. Its capacitance decay in the following 9000 cycles is about 4.4%, which is just slightly lower than that (2.5%) of the TS-rGO(700) material.

In order to give a reasonable interpretation of the cycle performance improvement induced by the thermal treatment, the high-resolution N1s and O1s XPS profiles of all the samples are fitted as shown in Fig. 5 and S7,<sup>†</sup> respectively. In N-doped carbonaceous materials, the nitrogen atoms usually exist in the forms of pyridinic N (N6 at about  $398.4 \pm 0.2 \text{ eV}$ ), pyrrolic/pyridonic N (N5 at about  $400.1 \pm 0.2 \text{ eV}$ ), quaternary N (NQ at about  $401.4 \pm 0.5 \text{ eV}$ ) and oxidized N (NX at about 402–405 eV),<sup>26,27,33</sup> which are schematically illustrated in the inset of Fig. 5b. According to the fitted results of the N1s XPS profiles as shown in Fig. 5 and Table 2, the doped nitrogen atoms in pristine C-rGO are almost pyrrolic/pyridonic ones. N6 and NQ atoms appear when the heating temperature rises to 500 °C and 600 °C respectively, and the NX atoms are always undetected at any heating temperature. Moreover, the relative percentage of both N6 and NQ increased with the rise in the heating temperature, while the variation of N5 is on the contrary. For example, the relative contents of N6, NQ and N5 are about 43.1%, 26.8% and 30.1% (Table 2 and Fig. 5b), respectively, when the heating temperature is 700 °C.

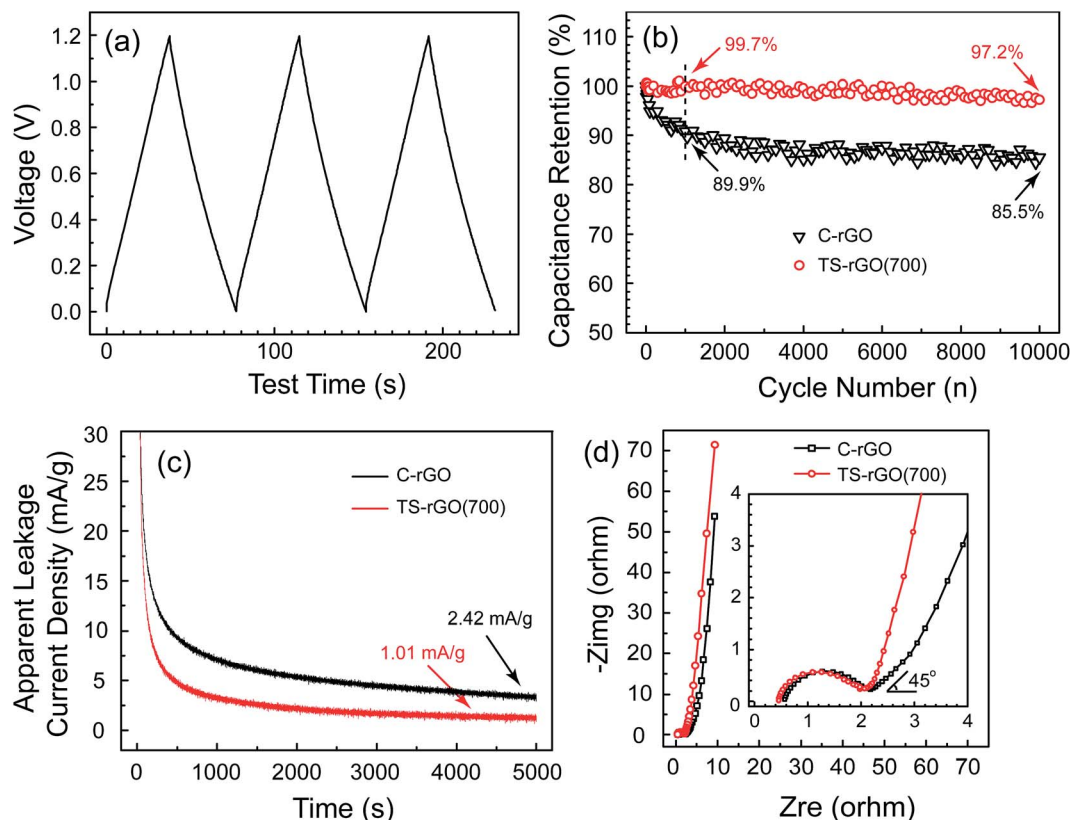
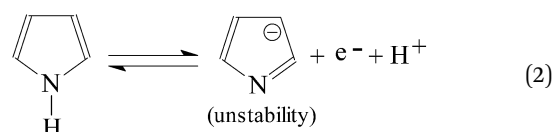


Fig. 4 (a) Galvanostatic charge/discharge curve of TS-rGO(700) at a current density of  $2 \text{ A g}^{-1}$ . Comparison of (b) cycling performance, (c) leakage current and (d) EIS Nyquist plots for C-rGO and TS-rGO(700). Inset of (d): partly enlarged Nyquist plots at a high frequency range.

It can be rationally deduced that the improper nitrogen functionalities, which exist in the pristine C-rGO material may be the main cause of inducement of the poor cycling performance, especially the huge decay of specific capacitance in the initial cycles, from the combination of the test results of N1s XPS fitting, CV and galvanostatic charge/discharge cycles. The unfavorable and detrimental cathodic peaks at  $0-0.1 \text{ V vs. SCE}$  in the CV curves as mentioned above (Fig. 3a and S6a†) should be ascribed to the electrochemical activities of the nitrogen functionalities. For the N5 functionalities, the possible redox reactions as illustrated in eqn (2) and (3), take place when the N-doped graphene materials are tested as electrode materials for SCs in  $1 \text{ mol L}^{-1} \text{ H}_2\text{SO}_4$  aqueous solution.<sup>32,34–36</sup> In the processes of the reactions, the five-membered pyrroles will be charged and may be gradually transformed into six-membered species due to its higher stability, whereas pyridonic groups charge into pyridinic ones, which will result in the reversible redox reactions as illustrated in eqn (4), to contribute the pseudocapacitance.<sup>37</sup> The fitting results of the N1s XPS profiles demonstrate that the nitrogen functional groups in the pristine C-rGO materials are the electrochemically unstable N5 species. Therefore, it exhibits unfavorable cycling performance in the initial cycles due to the irreversible changes of the N5 species, and then good cycle life in the following cycles after total transformation of the N5 species to stable ones. For the TS-rGO materials, the nitrogen functionalities are

optimized in the thermal stabilization processes, *i.e.*, the unstable N5 structures gradually transform to stable N6 and NQ structures along with the rise of the heating temperature, thus making the irreversible cathodic peaks, which are centred at about  $0-0.1 \text{ V vs. SCE}$  in the CV curves disappear (Fig. 3b and S6b†) and hence improving the cycle stability of the rGO based materials (Fig. 4b). We also found that the higher the heating temperature, the better the cycling performance. In addition to the optimization of functional groups, the change of specific surface area (SSA) in the heating processes may be responsible for the enhancement of the electrochemical properties. Hence, we further performed tests to obtain  $\text{N}_2$  adsorption/desorption isotherms, which are shown in Fig. S4.† By fitting the isotherms, it is found that the SSA values just increase slightly along with the heating temperature. In other words, the nearly constant SSA of all the products should not be one of the major factors for the improvement of the electrochemical properties when the as-prepared rGO are used as electrode materials for SCs.



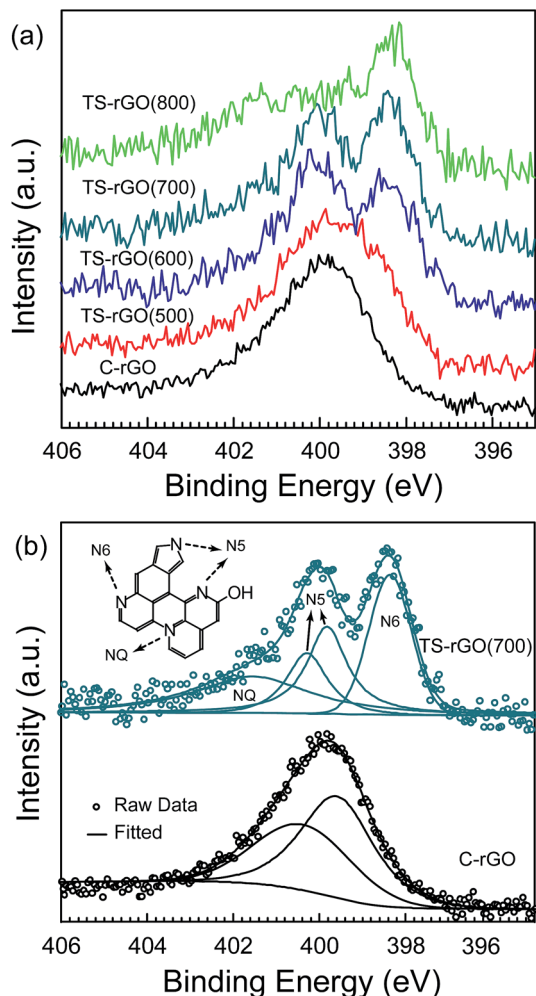
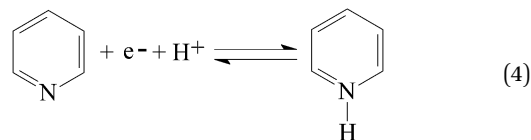
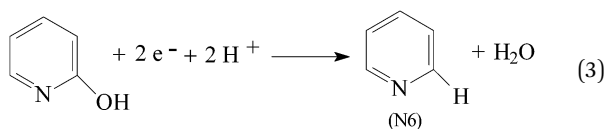


Fig. 5 (a) Comparisons of N1s XPS profiles of C-rGO and TS-rGO materials prepared at various temperature from 500 °C to 800 °C. (b) The experimental and fitted N1s XPS profiles of C-rGO and TS-rGO(700). Inset of (b): a schematic illustration of N-containing groups in carbonaceous materials.

Table 2 Atomic percentages of surface nitrogen species calculated from the N1s XPS fitting

Samples	Atomic% of nitrogen species		
	N6	N5	NQ
C-rGO	N.A.	100	N.A.
TS-rGO(500)	28.6	71.4	N.A.
TS-rGO(600)	40.7	44.3	15.0
TS-rGO(700)	43.1	30.1	26.8
TS-rGO(800)	46.3	15.4	38.3



In addition to the improvement of cycling performance, the thermal stabilization can also enhance the other electrochemical properties of rGO-based materials as electrode materials for SCs, including decrease of leakage current and increase of electrical conductivity. Leakage current is another important factor to evaluate the electrochemical stability of SCs, which is related to the structures of electrode materials to a certain extent, although it was seldom mentioned in previously reported papers.<sup>38</sup> In the present work, it is excitingly found that the apparent leakage current density of symmetrical rGO-based two-electrode SCs can be significantly reduced by thermally treating the active C-rGO materials. Taking the TS-rGO(700) material as an example, its apparent leakage current density (1.01 mA g<sup>-1</sup>) is much lower than that (2.42 mA g<sup>-1</sup>) of the C-rGO material (Fig. 4c), implying that the thermally stabilized r-GO materials can exhibit a higher energy efficiency and lower self-discharge rate when used as electrode materials for SCs compared to the pristine C-rGO material.

Furthermore, EIS spectra are further employed to compare the kinetic features of ion diffusion in C-rGO and TS-rGO(700) electrodes. As shown in Fig. 4d, both are characteristic Nyquist plots with almost vertically straight lines at low frequency (a typical double-layer capacitance), 45° slope at medium frequency (Warburg impedance), and semicircle at high frequency (charge transfer resistance).<sup>39</sup> The *x*-axis intercepts for C-rGO and TS-rGO(700) are 0.57 Ω and 0.46 Ω, respectively, demonstrating that the internal or equivalent series resistance of the TS-rGO(700) electrode is lower than that of the C-rGO electrode. It may be a result from the higher electrical conductivity of the TS-rGO(700) material compared to the C-rGO material. The shorter 45° Warburg line for TS-rGO(700) further signifies the faster kinetics of ion transfer.<sup>39</sup> The radii of the semicircle at high frequency for the C-rGO and TS-rGO(700) electrodes are almost equivalent, indicating the comparable charge transfer resistance.

Although thermal stabilization can effectively improve the high-rate and cycling performance and decrease the leakage current density as discussed above, it unfortunately reduces the specific capacitance of rGO based materials. In addition, the values of specific capacitance are negatively correlated to the heating temperature. According to the calculated results from the CV curves, the pristine C-rGO material can deliver a specific capacitance of about 210 F g<sup>-1</sup> at a scan rate of 1 mV s<sup>-1</sup>, which is reduced to about 187, 178, 165 and 142 F g<sup>-1</sup> at the heating temperature of 500, 600, 700 and 800 °C, respectively. A similar variation of the energy and power densities along with the heating temperature, compared to the specific capacities, is also obtained from the galvanostatic charge/discharge tests of the two-electrode systems. As shown in Fig. 6, the Ragone plots display the relationship between the energy density and power density. At relatively low power densities, the energy densities of



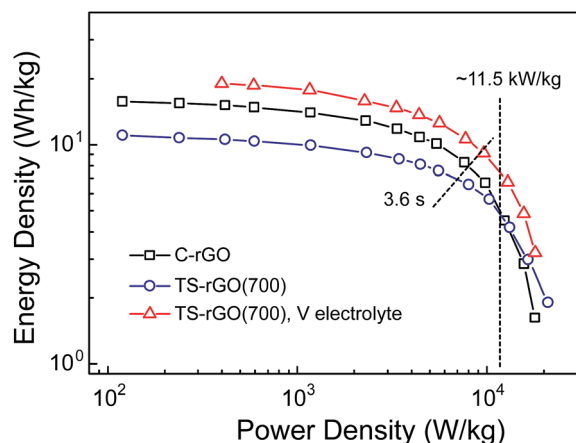


Fig. 6 Comparison of Ragone plots for C-rGO and TS-rGO(700).

the TS-rGO(700) material are slightly lower than those of pristine C-rGO, *e.g.*, the energy densities of the TS-rGO(700) and C-rGO materials are 11.0 and 15.7 W h kg<sup>-1</sup>, respectively at a power density of about 120 W kg<sup>-1</sup>. Fortunately, the TS-rGO(700) material delivers higher energy densities compared to pristine C-rGO when the power density is higher than 11.5 kW kg<sup>-1</sup> (Fig. 6), which is consistent with the CV test results, which show that the thermal stabilization can enhance the high-rate properties of rGO materials (Fig. 3c).

The reduced energy density in the heating processes can be significantly compensated by the pseudocapacitance of a redox-couple-added electrolyte, as illustrated in many reported papers.<sup>40–45</sup> Here, 0.1 mol L<sup>-1</sup> VOSO<sub>4</sub> and NH<sub>4</sub>VO<sub>3</sub> were simultaneously added into 1 mol L<sup>-1</sup> H<sub>2</sub>SO<sub>4</sub> solution, forming the redox active electrolyte, which can remarkably increase the energy and power densities of the TS-rGO materials to a higher level. As seen in the two Ragone plots of the TS-rGO(700) materials shown in Fig. 6, the energy and power densities of the 0.1 mol L<sup>-1</sup> VO<sup>2+</sup>/VO<sub>3</sub><sup>-</sup> couple system, which was added, are about 9.35 W h kg<sup>-1</sup> and 9.5 kW kg<sup>-1</sup>, respectively, both of which are higher than those (6.86 W h kg<sup>-1</sup> for energy density and 7.0 kW kg<sup>-1</sup> for power density) of the pristine electrolyte system, when the charge/discharge process was completed in 3.6 s. The increased energy and power densities originate from the redox-active electrolyte derived pseudocapacitance as clearly illustrated in Fig. S8.†

## 4. Conclusions

In summary, it is found that the cycle performance of a commercial N-doped rGO material prepared from the modified Hummers method is unsatisfactory when used as an electrode material for SCs, mainly due to huge decay of specific capacitance in the initial cycles, which has already been displayed but not discussed in some previously reported papers. In this paper, we studied the reasons, which led to the unfavorable cycle performance and successfully developed a thermal stabilization method to enhance the cycling properties of C-rGO based materials. We found that, the doped nitrogen atoms of pyrrolic/

pyridonic structures may be the main factor causing the initial decay of specific capacitance because of their instability in the cycling process. After the thermal stabilization treatment, these unstable functionalities transformed into more stable ones (pyridinic and quaternary nitrogen), and the corresponding cycle performance is significantly improved, *e.g.*, the 10 000<sup>th</sup> cycle capacitance retention of the 700 °C TS-rGO sample is up to 97.2%, which is much higher than that (85.5%) of pristine C-rGO. In addition to the enhanced cycle performance, the thermal stabilization process can also improve the high-rate capacitance, decrease the leakage current and impedance, and increase the power density. Furthermore, the unfortunately reduced energy density can be compensated by the pseudocapacitance of a redox-couple-added electrolyte to a higher level. This study not only provides a simple and mass-producible method to improve the electrochemical properties of rGO based materials as electrode materials for supercapacitors, especially the cycle performance, but also gives clear understanding of the probable reasons of improvement.

## Acknowledgements

This work was supported by the National Natural Science Foundation of China (grant number: 51102042), the Fundamental Research Funds for the Central Universities (14QNJJ014), the Science Technology Program of Jilin Province (20140101087JC, 20150520027JH), the National High Technology Research and Development Program of China (SS2012AA110301, 2013AA110103). XL thanks the support of the International Postdoctoral Exchange Fellowship Program.

## Notes and references

- 1 P. Simon, Y. Gogotsi and B. Dunn, *Science*, 2014, **343**, 1210–1211.
- 2 J. B. Goodenough, *Energy Environ. Sci.*, 2014, **7**, 14–18.
- 3 H.-G. Jung, N. Venugopal, B. Scrosati and Y.-K. Sun, *J. Power Sources*, 2013, **221**, 266–271.
- 4 F. Beguin, V. Presser, A. Balducci and E. Frackowiak, *Adv. Mater.*, 2014, **26**, 2219–2251.
- 5 S. Lü, C. Wang and X.-T. Wang, *J. Mol. Sci.*, 2013, **29**, 290–293.
- 6 P. Simon and Y. Gogotsi, *Acc. Chem. Res.*, 2013, **46**, 1094–1103.
- 7 V. Augustyn, P. Simon and B. Dunn, *Energy Environ. Sci.*, 2014, **7**, 1597–1614.
- 8 C. Cui, W. Qian, Y. Yu, C. Kong, B. Yu, L. Xiang and F. Wei, *J. Am. Chem. Soc.*, 2014, **136**, 2256–2259.
- 9 Y. Zhou, S. L. Candelaria, Q. Liu, Y. Huang, E. Uchaker and G. Cao, *J. Mater. Chem. A*, 2014, **2**, 8472–8482.
- 10 R. Wang, J. Lang and X. Yan, *Sci. China: Chem.*, 2014, **57**, 1570–1578.
- 11 L. Qie, W. Chen, H. Xu, X. Xiong, Y. Jiang, F. Zou, X. Hu, Y. Xin, Z. Zhang and Y. Huang, *Energy Environ. Sci.*, 2013, **6**, 2497–2504.
- 12 B. Liu, H. Shioyama, T. Akita and Q. Xu, *J. Am. Chem. Soc.*, 2008, **130**, 5390–5391.
- 13 J. Liu, *Nat. Nanotechnol.*, 2014, **9**, 739–741.



- 14 M. D. Stoller, S. Park, Y. Zhu, J. An and R. S. Ruoff, *Nano Lett.*, 2008, **8**, 3498–3502.
- 15 J. Zhu, D. Yang, Z. Yin, Q. Yan and H. Zhang, *Small*, 2014, **10**, 3480–3498.
- 16 W.-Y. Tsai, R. Lin, S. Murali, L. L. Zhang, J. K. McDonough, R. S. Ruoff, P.-L. Taberna, Y. Gogotsi and P. Simon, *Nano Energy*, 2013, **2**, 403–411.
- 17 Y. Yan, Y.-X. Yin, Y.-G. Guo and L.-J. Wan, *Adv. Energy Mater.*, 2014, **4**, 1301580.
- 18 A. Zurutuza and C. Marinelli, *Nat. Nanotechnol.*, 2014, **9**, 730–734.
- 19 H. M. Jeong, J. W. Lee, W. H. Shin, Y. J. Choi, H. J. Shin, J. K. Kang and J. W. Choi, *Nano Lett.*, 2011, **11**, 2472–2477.
- 20 L. L. Zhang, X. Zhao, H. Ji, M. D. Stoller, L. Lai, S. Murali, S. McDonnell, B. Cleveger, R. M. Wallace and R. S. Ruoff, *Energy Environ. Sci.*, 2012, **5**, 9618–9625.
- 21 Y. Zhu, S. Murali, M. D. Stoller, K. J. Ganesh, W. Cai, P. J. Ferreira, A. Pirkle, R. M. Wallace, K. A. Cychosz, M. Thommes, D. Su, E. A. Stach and R. S. Ruoff, *Science*, 2011, **332**, 1537–1541.
- 22 X. Wang, Y. Zhang, C. Zhi, X. Wang, D. Tang, Y. Xu, Q. Weng, X. Jiang, M. Mitome, D. Golberg and Y. Bando, *Nat. Commun.*, 2013, **4**, 2905.
- 23 X. Yang, C. Cheng, Y. Wang, L. Qiu and D. Li, *Science*, 2013, **341**, 534–537.
- 24 Y. Wang, Z. Shi, Y. Huang, Y. Ma, C. Wang, M. Chen and Y. Chen, *J. Phys. Chem. C*, 2009, **113**, 13103–13107.
- 25 S. Ye, J. Feng and P. Wu, *ACS Appl. Mater. Interfaces*, 2013, **5**, 7122–7129.
- 26 J. H. Lee, N. Park, B. G. Kim, D. S. Jung, K. Im, J. Hur and J. W. Choi, *ACS Nano*, 2013, **7**, 9366–9374.
- 27 Z. Li, Z. Xu, H. Wang, J. Ding, B. Zahir, C. M. B. Holt, X. Tan and D. Mitlin, *Energy Environ. Sci.*, 2014, **7**, 1708–1718.
- 28 X. Zhou, Y.-X. Yin, L.-J. Wan and Y.-G. Guo, *Adv. Energy Mater.*, 2012, **2**, 1086–1090.
- 29 K. Parvez, Z.-S. Wu, R. Li, X. Liu, R. Graf, X. Feng and K. Müllen, *J. Am. Chem. Soc.*, 2014, **136**, 6083–6091.
- 30 N. Xiao, H. Tan, J. Zhu, L. Tan, X. Rui, X. Dong and Q. Yan, *ACS Appl. Mater. Interfaces*, 2013, **5**, 9656–9662.
- 31 H. A. Andreas and B. E. Conway, *Electrochim. Acta*, 2006, **51**, 6510–6520.
- 32 Y.-H. Lee, K.-H. Chang and C.-C. Hu, *J. Power Sources*, 2013, **227**, 300–308.
- 33 J. Machnikowski, B. Grzyb, J. V. Weber, E. Frackowiak, J. N. Rouzaud and F. Béguin, *Electrochim. Acta*, 2004, **49**, 423–432.
- 34 E. Frackowiak, G. Lota, J. Machnikowski, C. Vix-Guterl and F. Béguin, *Electrochim. Acta*, 2006, **51**, 2209–2214.
- 35 G. Lota, K. Lota and E. Frackowiak, *Electrochem. Commun.*, 2007, **9**, 1828–1832.
- 36 E. Frackowiak, *Phys. Chem. Chem. Phys.*, 2007, **9**, 1774–1785.
- 37 D.-W. Wang, F. Li, L.-C. Yin, X. Lu, Z.-G. Chen, I. R. Gentle, G. Q. Lu and H.-M. Cheng, *Chem.-Eur. J.*, 2012, **18**, 5345–5351.
- 38 X.-G. Zhuang, Y.-S. Yang, D.-P. Yang, Y.-J. Ji and Z.-Y. Tang, *Battery*, 2003, **33**, 199–202.
- 39 X.-L. Wu, W. Wang, Y.-G. Guo and L.-J. Wan, *J. Nanosci. Nanotechnol.*, 2011, **11**, 1897–1904.
- 40 E. Frackowiak, K. Fic, M. Meller and G. Lota, *ChemSusChem*, 2012, **5**, 1181–1185.
- 41 L. Chen, H. Bai, Z. Huang and L. Li, *Energy Environ. Sci.*, 2014, **7**, 1750–1759.
- 42 C. Zhao, W. Zheng, X. Wang, H. Zhang, X. Cui and H. Wang, *Sci. Rep.*, 2013, **3**, 2986.
- 43 S. T. Senthikumar, R. K. Selvan, Y. S. Lee and J. S. Melo, *J. Mater. Chem. A*, 2013, **1**, 1086–1095.
- 44 S. T. Senthikumar, R. K. Selvan, N. Ponpandian, J. S. Melo and Y. S. Lee, *J. Mater. Chem. A*, 2013, **1**, 7913–7919.
- 45 H. Yu, J. Wu, L. Fan, Y. Lin, S. Chen, Y. Chen, J. Wang, M. Huang, J. Lin, Z. Lan and Y. Huang, *Sci. China: Chem.*, 2012, **55**, 1319–1324.